# EFFECT OF FREE-STREAM TURBULENCE ON FLOW OVER AEROFOIL SECTION AT HIGH INCIDENCE

T. K. Sengupta†, S. De and K. Gupta

*Department of Aerospace Engineering, Indian Institute of Technology Kanpur*
*Kanpur 208 016, India*

Unsteady flow past a NACA 0015 aerofoil is investigated for moderate Reynolds numbers at high angles of attack by solving the full 2-D Navier–Stokes equations with and without the presence of free-stream turbulence (FST). The investigation focusses on the *by-pass* mode of transition usually encountered in turbomachinery and wind engineering where the flow field around a bluff-body can experience very high levels of FST. In this study, a 5% level of FST is considered. While FST is all-pervasive, its effect has not been studied at all theoretically. Here, this has been made possible by proposing a new model for FST based on a moving-average time-series and using it for long-time computation of the Navier–Stokes equations. The statistics of the modelled FST follows the statistics of a specific wind tunnel. The use of this model in conjunction with higher order upwinding, for the convection term to model the vorticity dynamics, gives the solution a very high degree of accuracy in the *by-pass* transitional flow regime. The present study is relevant for understanding the implications of reduced order modelling proposed for aeroelastic studies. The numerical results view the solution of the Navier–Stokes equations not only as the output of a dynamical system in the presence of stochastic noise (FST), but which also produces the intermittency factor in and around the aerofoil dominated by differing pressure gradient and unsteady effects. The last attribute is also a novel feature of the present study and is relevant to bluff-body flow fields. The computed flow field shows that the flow achieves a statistical stationarity even though the overall flow is chaotic and aperiodic. © 2001 Academic Press

## 1. INTRODUCTION

FLUID FLOW TRANSITION from the laminar to the turbulent state usually begins because of the receptive nature of the underlying shear layer. The ability of the shear layer to respond and amplify certain frequencies and wavelengths of present disturbances (noise) is distinct from the buffeting problem. After the initial receptivity stages, the generated disturbance field is amplified under proper conditions. When the background noise is small in magnitude, various three-dimensionalities and nonlinearities cause this amplification process to saturate, leading to turbulence. However, when the level of disturbance is very high—as in the present case—a *by-pass* transition is observed, where the usual amplfication of unstable Tollmien–Schlichting waves is *by-passed*, in which case, various other mechanisms are seen to exist [see, e.g., Wu *et al.* (1999) and Sengupta *et al.* (1999)].

The power spectra of turbulent flows are broadband, and are known to be aperiodic, i.e., neither stochastic nor multiply periodic (Vastano & Moser 1991). Since dissipative nonlinear systems also display aperiodic motion in phase-space attractors, it is quite natural to

---

† Currently Senior Visiting Fellow at National University of Singapore.

investigate such systems using deterministic chaotic tools. The verification of the above ideas first came in a series of experiments on internal flows, namely for the Taylor–Couette flows by Gollub and co-workers (Gollub & Swinney 1975; Fenstermacher *et al.* 1979). Similar evidence has been displayed for other internal flows through numerical simulations of the Navier–Stokes equation depicting uniform flow past bodies without the presence of any extrinsic noise. These include the Taylor–Couette flow by Vastano and Moser (1991) and flow in cascades by Fortin *et al.* (1987).

Pulliam & Vastano (1993) were the first to report low-dimensional chaotic behaviour of an unforced open flow. In that numerical study the flow past a NACA 0015 aerofoil at a large angle of attack ($\alpha = 30°$) was investigated to determine the bifurcation sequence as Reynolds numbers were increased from very small values up to 3000. Also, some quantitative measure of chaos of the aperiodic flow was presented via time delay phase-space portraits and Lyapunov exponents. In earlier work, Fortin *et al.* (1987) performed finite-element simulation of incompressible flow in a cascade. However, the grid used was too coarse to separate the physical sequence of bifurcations from numerical effects. The studies of both Pulliam & Vastano (1993) and Fortin *et al.* (1987) indicated the sequence of bifurcations and the presence of newer and newer frequencies in the frequency spectrum. In these studies the presence of noise was not considered, and the sequence of bifurcations leading to *turbulence* was triggered by computational round-off and other numerical errors. For the cascade flow, the first periodic doubling was observed at Re = 1200 with the next period doubling at Re = 1900. At Re = 2200 the frequency spectrum was *continuous*. For the external flow problem in Pulliam & Vatsano (1993), a much more detailed study revealed the first period doubling at Re = 1075. Figure 2 of the same reference indicates detection of up to period-64 solution for Reynolds numbers between 1580 and 1583. It is to be mentioned here that the grids used by Pulliam & Vastano (1993) were much finer (coarsest grid of size $169 \times 49$) as compared to $8 \times 49$ grid used in Fortin *et al.* (1987). After the period-64 motion, as the Reynolds number was further increased, *a series of chaotic states interspersed with periodic windows* was detected in Pulliam & Vastano (1993). However, it was stated in Pulliam & Vastano (1993) that the bifurcation sequence somewhat changed when finer grids (of size $369 \times 89$ and $849 \times 161$) were used. The bifurcation sequence and transition to chaos changed further when higher-order accurate TVD schemes were used. However, the importance of these studies lay in the fact that period-doubling and the bifurcation sequence were demonstrated with the help of the full Navier–Stokes equations and not by model difference equations, as employed in the study of chaotic dynamics.

It is often stated that the flow at high Reynolds numbers ought to be three-dimensional because 3-D flows have the known energy cascade mechanism via vortex stretching. At the same time previous 2-D numerical simulations, including the present one, clearly demonstrate that energy can cascade via period-doubling bifurcations for 2-D flows. The role of nonlinearity in generating vortices of smaller scale from shear layers characterized by large-scale vorticity was also demonstrated by Legras & Dritchel (1993) in the context of a discrete vortex method computation of inviscid flows in two dimensions. The phenomenon of *vortex stripping*, alluded to above, is a clear demonstration that there are indeed other energy cascade mechanisms. In another study related to the receptivity aspect of zero pressure gradient flows to free-stream disturbances, it has been demonstrated by Sengupta *et al.* (1999) that, even in the context of linearized dynamics, the viscous flow shows an energy cascade via dispersion effects even though the flow may not be unstable.

All the above numerical works, except the one by Sengupta *et al.* (1999), relate to intrinsic dynamics, i.e. there are no disturbances driving the fluid dynamical system. No effort has been made to date to study the extrinsic dynamics of a fluid dynamic system (stochastic

system) governed by the Navier–Stokes equations. By definition, a stochastic system is one that is subjected to *random* external forcing. Although such studies have been made via the direct interaction approximation (DIA), that can be viewed as asymptotically exact solution of the Navier-Stokes equation [see Frisch (1995) for a discussion], the interest here is to study numerically the flow past an aerofoil at large angles of attack and at higher Reynolds numbers in the presence of FST. The present choice of Reynolds numbers (35 000 and 100 000) is deliberate, as the effect of nonlinear terms is to render any periodic solution unstable for certain parameter choices (in this case the Reynolds number). Although the nonlinearity does not guarantee chaos, it does make the existence of chaos possible.

The problem of diagnostics of oncoming noise fields and impurities is important, as the strong inhomogeneities of the mean flow produce significant straining of the disturbance field as they approach the body and the shear layer. It is expected that the present study will reveal some of these important effects of the flow. In an actual flow-field the omnipresent background noise like FST actually triggers transition to turbulence. For example, in compressor and turbine cascades it is common to find high levels of (1–5%) turbulence intensity. This effect has not been studied earlier, despite its tremendous practical importance, perhaps due to the absence of a proper model of FST along with an accurate Navier–Stokes solver that does not suffer from numerical uncertainties. In Section 2, a new model for FST based on a Moving Average (MA) time-series method is proposed. The governing equation and the adopted numerical methods for the accurate higher-order upwind scheme are briefly discussed in Section 3. The results and discussion are given in Section 4 followed by conclusions.

## 2. MODELLING FREE-STREAM TURBULENCE

There is a genuine need to model the background noise that is omnipresent in any fluid dynamic system. For aerospace applications these noise sources are (i) acoustic, (ii) vortical and (iii) entropic in origin. In the present exercise, the acoustic and vortical components of the background noise are modelled—as they are important for incompressible flows. There has been some limited success, reported by Atassi (1994), in the development of aerodynamic theories of streaming motions around bodies with unsteady vortical and entropic disturbance. However, these studies are essentially limited to linear and/or inviscid flows. The turbulence intensity considered in this present study is 5%. This value is typically on the high side for gas turbine applications, where inclusion of both nonlinear and viscous effects is mandatory.

If one measures the velocity signal in a wind tunnel and subtracts the mean flow component, then the signal appears to be highly disorganized and the detailed behaviour appears intractable. Despite this, it is possible to see some organization when the statistical properties are viewed. In Figure 1 the velocity signal from the S1 wind tunnel of ONERA is reproduced along with the corresponding histograms from Frisch (1995). These data have been treated as typical of similar wind tunnel facilities. Both the histograms have identical statistical properties, despite their different time origin, pointing to the utility of statistical information of the signal. Here the statistics is used to develop a time series to model the FST by following a standard moving average (MA) time-series method that can be found in Fuller (1978).

The disturbances represented by high-frequency fluctuations are due to many reasons and, if the contraction ratio upstream of the test-section is not high, then the disturbance field (which is the FST) is isotropic. Based on this assumption and the invariance of the noise statistics from the histogram in Figure 1, the vorticity that enters the domain of interest through the inflow boundary can be calculated.
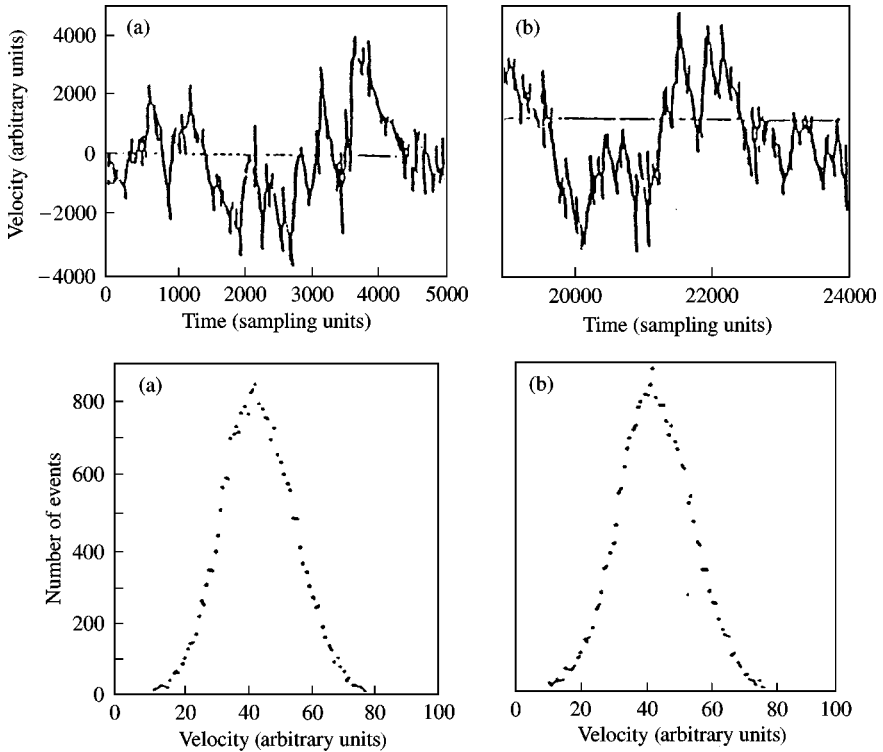
Figure 1. Streamwise fluctuating velocity data for ONERA S1 wind tunnel shown for two different time intervals.

From the histogram the first four moments are calculated from

$$\mu_n = \frac{\sum [f(x_i - \mu)]^n}{\sum f(x_i)},$$

(1)

where $f(x)$ is the function depicting the discrete data in the histogram in Figure 1. In this equation the superscript indicates the exponent of the shifted function. The shift is performed by the mean value of the function. The coefficient of skewness and kurtosis of the histogram are given by

$$\gamma_1 = \frac{\mu_3}{\mu_{3/2}^2}, \qquad \gamma_2 = \frac{\mu_4}{\mu_2^2} - 3.$$

(2,3)

In the development of the model, an important observation is that the third moment (skewness) calculated from the histogram is negligibly small. For one of the time series, it is a small positive number and for the other time series this is a small negative number. It has been shown in Frisch (1995), that the skewness is a measure of vortex stretching and, for homogeneous turbulence, the skewness ought to be negative (Batchelor & Townsend 1947) if the time rate of change of enstrophy due to nonlinear interactions is positive. Here, to generate a synthetic time series for the velocity components, at the inflow boundary points, the third moment is treated as zero. The generated time series for the velocity components at the inflow boundary, matched the coefficients given by equations (1)–(3). In the present

work, the standard moving average (MA) model of order one, as given in Fuller (1978), has been used:

$$x_t = e_t + \alpha_1 e_{t-1}, \tag{4}$$

where $e_t$'s are given by a normal distribution of zero mean and standard deviation $\sigma$. From the given histograms, shown in Figure 1, one can calculate the four moments of the input noise signal at the inflow boundary and they can be equated to the four moments of the time series given by equation (4). Thus one has two equations for the two unknowns $\alpha_1$ and $\sigma$. The time series given by (4) is valid only when noise signals are symmetric. To consider noise models with nonzero skewness, one has to develop models that are inherently asymmetric.

The various moments of equation (4) are given by

$$\mu_1 = E(x_t) = 0, \qquad \mu_2 = E(x_t^2) = (1 + \alpha_1^2)\sigma^2, \tag{5,6}$$

$$\mu_3 = E(x_t^3) = 0, \qquad \mu_4 = E(x_t^4) = (1 + \alpha_1^4)3\sigma^4, \tag{7,8}$$

The time series, represented by Equation (4), produces isotropic velocity fluctuation due to FST. It is furthermore assumed that during the initial phase, when the oncoming flow is accelerated, the noise will not be stationary and the instantaneous standard deviation of the velocity signal will follow (a form) dictated by equation (11).

## 3. GOVERNING EQUATION AND NUMERICAL METHOD

The governing equation of motion for the 2-D flow is given by the Navier–Stokes equations. In the stream function–vorticity formulation, these are given by

$$\nabla_{2D}^2 \psi = -\omega, \tag{9}$$

$$\frac{\partial \omega}{\partial t} + \nabla_{2D}(\omega \mathbf{V}) = \frac{1}{\text{Re}} \nabla_{2D}^2 \omega, \tag{10}$$

where $\text{Re} = U_\infty c/v$, with $U_\infty$ being the final free-stream speed and $c$ the chord of the airfoil. The choice of the $(\psi - \omega)$ formulation is (for achieving) higher accuracy. The existence of stream function satisfies mass conservation everywhere in the flow-field and thereby removes one of the major sources of error of solving the Navier–Stokes equation in primitive variable formulation. Also, such a formulation can be computed fast as pressure is not computed explicitly. The pressure field, whenever necessary, can be computed by solving the pressure Poisson equation separately–as has been done in Nair and Sengupta (1997) for elliptic cylinders.

One of the major aims here is to obtain time-accurate solution of the Navier–Stokes equation when the free-stream start-up process is well defined. Morikawa & Gronig (1995) have reported experimental results at $\text{Re} = 35\,000$ for flow past a NACA 0015 aerofoil for which the tunnel test-section speed history was provided. The free-stream speed achieved its final value ($U_\infty$) following

$$u_\infty(t = U_\infty \tanh\left(\frac{t}{\tau}\right). \tag{11}$$

Equations (9) and (10) are solved in an orthogonal transformed plane and they are given by

$$\frac{\partial}{\partial \xi}\left(\frac{h_2}{h_1}\frac{\partial \psi}{\partial \xi}\right) + \frac{\partial}{\partial \eta}\left(\frac{h_1}{h_2}\frac{\partial \psi}{\partial \eta}\right) = -h_1 h_2 \omega, \tag{12}$$

$$h_1 h_2 \frac{\partial \omega}{\partial t} + h_2 u \frac{\partial \omega}{\partial \xi} + h_1 v \frac{\partial \omega}{\partial \eta} = \frac{1}{\text{Re}}\left[\frac{\partial}{\partial \xi}\left(\frac{h_2}{h_1}\frac{\partial \omega}{\partial \xi}\right) + \frac{\partial}{\partial \eta}\left(\frac{h_2}{h_1}\frac{\partial \omega}{\partial \omega}\right)\right], \tag{13}$$

where $h_1$ and $h_2$ are the scale factors of the orthogonal transformation in the azimuthal and wall-normal ($\xi$, $\eta$) directions of the chosen O-grid topology. The grid generation strategy and details are given in Nair & Sengupta (1998) and is not repeated here. To solve equation (12), a grid is chosen in such a way that the truncation and aliasing errors (in evaluating the self-adjoint product terms) are minimized. The role of aliasing error in a linear equation has not been reported in the literature before for finite difference and finite volume computations. A look at (12) reveals that this is due to evaluation of the product terms on the left-hand side and thus depends on the scale factor ($h_1$, $h_2$) distribution in the transformed plane. Equation (12) is solved by the alternate direction implicit (ADI) method [see Nair & Sengupta (1997) for details]. The vorticity transport equation (13) is solved by discretizing the nonlinear convection terms by higher-order upwinding, while the dissipation terms are discretized using a second-order central difference scheme. The time advancement is by Euler time stepping in an explicit manner, for reasons of numerical stability and accuracy. For the accurate simulation of the Navier–Stokes equations one must choose a numerical method that is neutrally stable and which in turn requires the choice of very small CFL number or time step. In the present set of computations the time step has been restricted to $\Delta t = 10^{-5}$ for this reason. The method of higher-order upwinding is equivalent to large Eddy simulation, since the third-order upwinding enhances the spectral resolution by 44% as compared with the usual second-order schemes and this aspect has been discussed in Sengupta & Nair (1999).

The computational domain and the close-up view of the O-grid used, of size $301 \times 401$, are shown in Figure 2(b). This grid was used for all computations except the case for Re = 35 000 for which another grid of size, $231 \times 301$, was used. These grids in the wall-normal direction are much finer than the one used by Pulliam & Vastano (1993), because of the enhanced requirements of resolution at higher Reynolds numbers of present simulations. This, together with the fact that higher-order upwinding has been used, provides high spectral accuracy of solutions at higher Reynolds numbers. The noise model described in the previous section allows one to fix the value of the time-dependent boundary conditions at the inflow of the computing domain shown in Figure 2(a). This is given by the following Neumann boundary conditions at the inflow:

$$\frac{\partial \psi}{\partial y} = u_\infty(t) + u'(t), \qquad \frac{\partial \psi}{\partial x} = -v'(t), \tag{14a, b}$$

where $u_\infty(t)$ is given by (11) and the fluctuating components of velocity ($u'(t)$, $v'(t)$) are given by the noise model described in the previous section, equation (4). The fluctuating disturbances that are introduced through the inflow boundary, subsequently, evolve as governed by the Navier–Stokes equations. There are no assumptions made for the noise model, except that no length scale of the FST is incorporated. This can be included if the information on length scale is available. The boundary condition for stream function on the surface of the aerofoil is given by

$$\psi = \text{const} \tag{15a}$$

On the cut (AF and CD) the periodic boundary conditions apply for all variables. The noise model also fixes the time-dependent vorticity boundary condition on the inflow as a Dirichlet boundary condition. For equation (13), at the outflow boundary, the diffusion operator is switched off, i.e. locally a Euler equation is solved.

The no-slip boundary condition on the wall fixes the wall vorticity, and this works as the major vorticity production term for the vorticity transport equation. This wall vorticity is
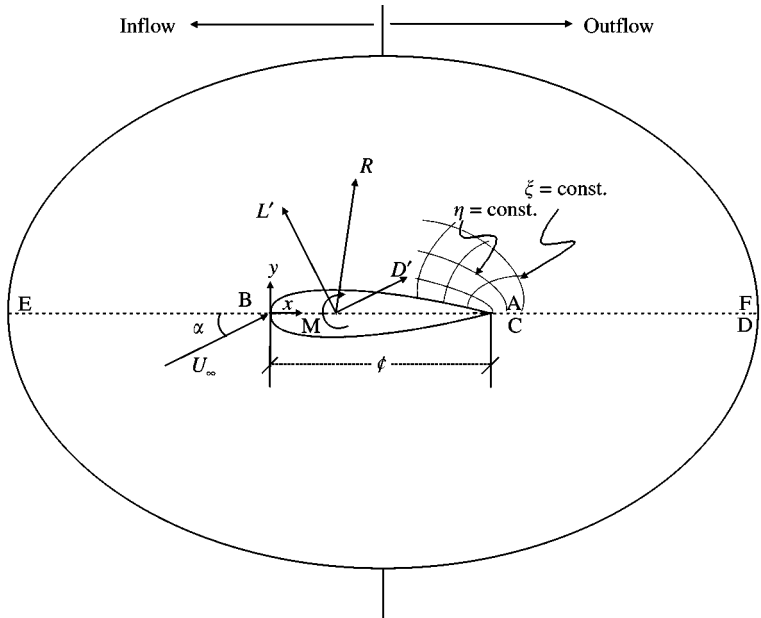
(a)
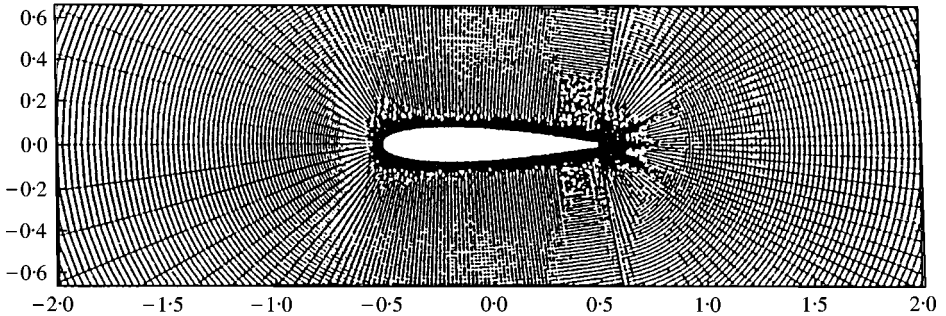


(b)

Figure 2(a). The schematic of the flow field with inflow and outflow boundary indicated. (b) Close-up view of the used O-grid of size (301 × 401) around NACA 0015. (c) The location of points where the velocity and vorticity data are stored.

calculated from equation (12) by applying the no-slip condition. The resultant expression for the time-dependent wall vorticity is given by

$$\omega_b = -\frac{1}{h_2^2}\frac{\partial^2 \psi}{\partial \eta^2}. \tag{15b}$$

## 4. RESULTS AND DISCUSSION

The effect of FST is studied for unsteady viscous flow around NACA 0015 via the solution of the full Navier–Stokes equations for Re = 3000, 35 000 and 100 000 at various angles of attack. The points at which the azimuthal and wall-normal velocity components and vorticity were stored, as a time series for the Reynolds numbers, are shown in Figure 2(c) and the corresponding coordinates are tabulated in Table 1. The points are chosen to provide insight into different flow regimes. For example, for Re = 35 000, Points 1, 4–7 are within the attached shear layer. Point 2 is located within the separated shear layer. Points 3,
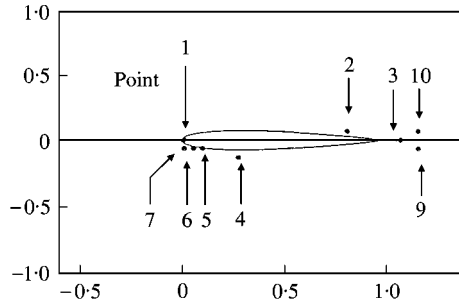
Points shown over the airfoil
NACA 0015 for Re = 35,000.
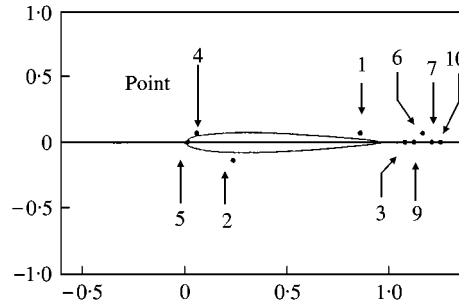
(c)

Points shown over the airfoil
NACA 0015 for other cases.

Figure 2 (continued)

TABLE 1

| Point No. | $x$ | $y$ |
|---|---|---|
| Sampling points for the Reynolds number = 35 000 | | |
| 1 | $-2·6175 \times 10^{-4}$ | $7·2478 \times 10^{-3}$ |
| 2 | 0·9652 | $8·1048 \times 10^{3}$ |
| 3 | 1·0012 | $4·5535 \times 10^{-5}$ |
| 4 | 0·5471 | $-6·2967 \times 10^{-2}$ |
| 5 | $1·4906 \times 10^{-2}$ | $-2·7320 \times 10^{-2}$ |
| 6 | $1·0299 \times 10^{-3}$ | $-1·0780 \times 10^{-2}$ |
| 7 | $-1·2570 \times 10^{-3}$ | $-1·1790 \times 10^{-2}$ |
| 9 | 1·0602 | $-8·0034 \times 10^{-3}$ |
| 10 | 1·0602 | $8·0034 \times 10^{-3}$ |
| Sampling points for all other Reynolds numbers | | |
| 1 | 0·9999 | 0·0008 |
| 2 | 0·3455 | $-0·0745$ |
| 3 | 1·0013 | 0·0000 |
| 4 | 0·0289 | 0·0363 |
| 5 | 0·0028 | $-0·0142$ |
| 6 | 1·0074 | 0·0002 |
| 7 | 1·0075 | 0·0000 |
| 9 | 1·0055 | 0·0000 |
| 10 | 1·0098 | 0·0000 |

9 and 10 are located in the near wake. Among Points 1, 4–7, the choice of location was dictated by the fact that each of these locations experiences a different pressure gradient. These have been chosen to explore whether the space–time dependence of the solutions at all these points can be separated simultaneously, so that reduced-order modelling for aeroelastic computations can be possible for bluff-body flows (Dowell 1996). The time series have been stored at these points to find the time limit up to which the computation should proceed to achieve statistical stationarity of the data. No effort has been made to calculate the time-dependent loads experienced by the aerofoil. The sampling rate of data in all the cases has been taken as $\Delta t_s = 0.002$. These computations are very expensive; for example, for the case of Re = 100 000, the total computation time is of the order of several thousands of CPU hours on SGI origin 200 when computed up to $t = 250$.

It is well known that low-dimensional nondissipative dynamical systems often display chaos, when some parameters are increased. The dynamical system theory as applied to fluid dynamics assumes intrinsic dynamics without any need to consider external noise. The present exercise is undertaken to study the extrinsic dynamics of flow past the aerofoil at high angles of attack, with respect to the effects of FST in the transitional and turbulent flow regimes. Even when the flow is given by intrinsic dynamics, the FST is needed to prevent the dynamical system from being trapped in one of many possible attractors with small basin. The statistical properties of the solution depend on the basin on which the initial and boundary conditions belong.

The case of a NACA 0015 airfoil at $\alpha = 20°$ without any noise was computed by Pulliam & Vastano (1993) for Re = 3000. To distinguish between extrinsic and intrinsic dynamics the same case has been computed here with 5% FST. For this case, the same fine grid that is employed for Re = 100 000 is used. An additional case at $\alpha = 30°$ was investigated for Re = 3000. Only the results are summarized, without showing any figures. It was noted that the presence of FST produces lower levels of disturbance at Point 1, while at Point 2, which is in the vicinity of the front stagnation point, the response-amplitude is least with and without noise. Furthermore, the bandwidth of response is wider for the case without noise. The Lyapunov exponents are shown in Table 2, for Re = 3000 and 35 000. The Lyapunov exponents have been calculated following the method of Wolf *et al.* (1985). The physical implications and the evaluation methods of Lyapunov exponent are also given in Baker & Gollub (1996). All the cases demonstrate the flow to be chaotic, as the Lyapunov exponents are all positive with the exception of Point 2, for Re = 3000 and $\alpha = 20°$, where the maximum Lyapunov exponent is found to be negative. This is consistent, since the point is located in the favourable pressure gradient zone for which the flow is stable. For $\alpha = 20°$, the maximum Lyapunov exponents range from $-0.0236$ at Point 2 to 0.1163 at Point 6. However, when the angle of attack was increased to $30°$, the maximum Lyapunov exponents increased at all points and are of the same order of magnitude. For Re = 35 000 the average Lyapunov exponent is lowest for Points 4 and 5.

Instead of showing the time series of all the points for all the cases, only the velocity components at some selected points are shown for the Re = 100 000 and $\alpha = 30°$ case. Figure 3(a) displays the u-component time series at all the nine points whose coordinates are given in Table 1. Points 3,9,6,7 and 10 are near a line along the streamwise direction and hence this velocity component denotes the normal velocity component, while for Points 1,2,4 and 5, this is the streamwise velocity component. For Point 5, which is in the vicinity of the front stagnation point, this velocity component exhibits large unsteady excursions over longer time intervals. Point 2, which is in a region of negative (favourable) pressure gradient exhibits a quiescent flow condition.

TABLE 2
Lyapunov exponents at different locations given in Table 1

| Point no. | With noise $\alpha = 20°$ | Without noise $\alpha = 30°$ |
|---|---|---|
| Lyapunov exponent ($\lambda$) for Re = 3000 | | |
| 1 | 0·0873 | 0·1633 |
| 2 | − 0·0236 | 0·1317 |
| 3 | 0·1036 | 0·1876 |
| 4 | 0·0771 | 0·1255 |
| 5 | 0·0629 | 0·1597 |
| 6 | 0·1163 | 0·1805 |
| 7 | 0·0943 | 0·1888 |
| 9 | 0·1123 | 0·1657 |
| 10 | 0·1086 | 0·1669 |

Lyapunov exponent ($\lambda$) for Re = 35 000

| Point no. | $\alpha = 30°$ |
|---|---|
| 1 | 0·2564 |
| 2 | 0·3628 |
| 3 | 0·2128 |
| 4 | 0·3631 |
| 5 | 0·3172 |
| 6 | 0·3163 |
| 7 | 0·3388 |
| 9 | 0·2580 |
| 10 | 0·3998 |

The velocity component time series can be expressed as

$$u(r, t) = \frac{1}{2\pi} \int (\hat{u}(r, \omega) e^{-i\omega t} \, d\omega$$

with $\hat{u}(r, \omega)$ as the Fourier amplitude of the signal and can be obtained by fast Fourier transform (FFT). The FFT has been obtained using the FFTW, version 2.0.1 software developed by Frigo & Johnson (1997). In Figure 3(b) this amplitude is plotted as a function of $\log_{10}(\omega)$. The choice of logarithmic scale is to highlight the lower frequencies. It is to be noted that the FST at inflow excites up to $\omega = 500$—the Nyquist limit corresponding to the sampling rate of the time series. It is known that the long-time behaviour is determined by the low-frequency content. The near absence of Fourier amplitude at Point 2 implies the absence of noise and chaos. Similarly, for Point 5, the low-frequency amplitude is predominant and the amplitude is almost zero beyond $\omega = 10$. The FFT of the signal for Points 1 and 3, indicates the behaviour of the shear layer under the action of an adverse pressure gradient. The constant tail of the response, at high $\omega$, can be detected at these two points. The presence of a solid boundary at Point 1, attenuates the high-frequency component, as compared to constant amplitude response for Point 3 at higher frequencies. For Point 4, the
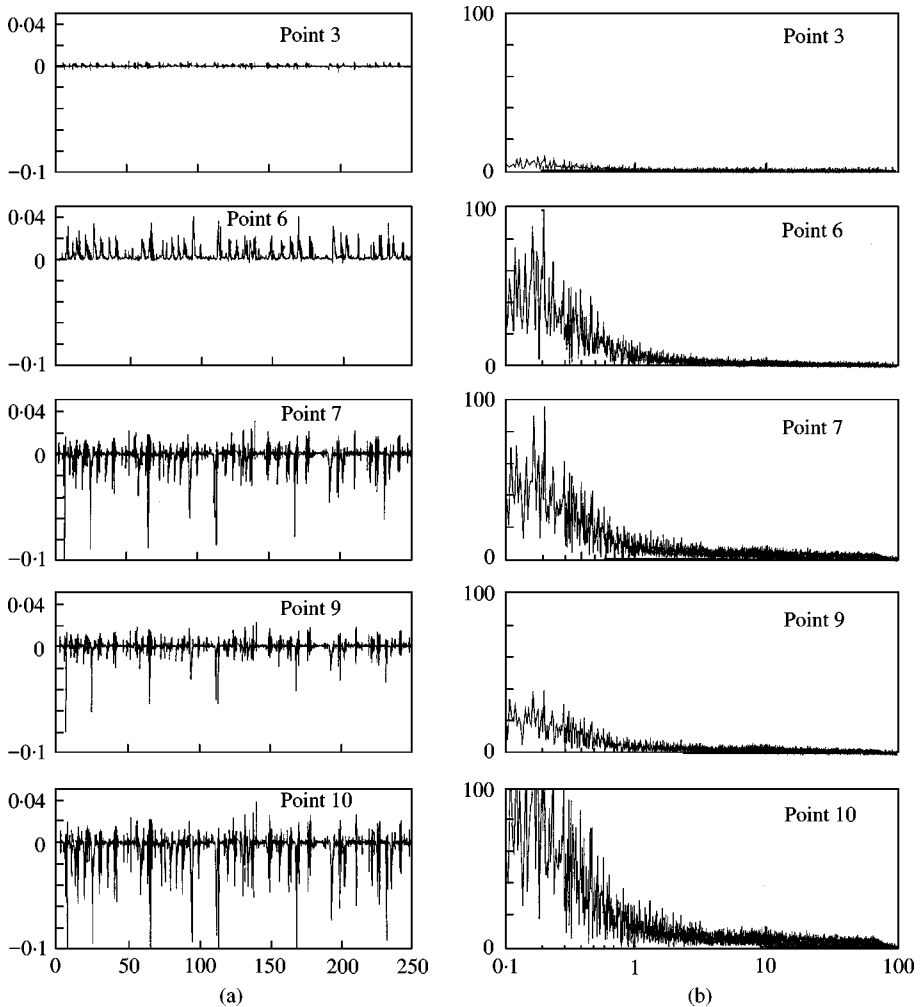
Figure 3 (a). The curvilinear u-component of velocity at the sampled points shown as a function of time. (b) The Fourier transform shown against frequency for the time series of (a).

(a)

(b)
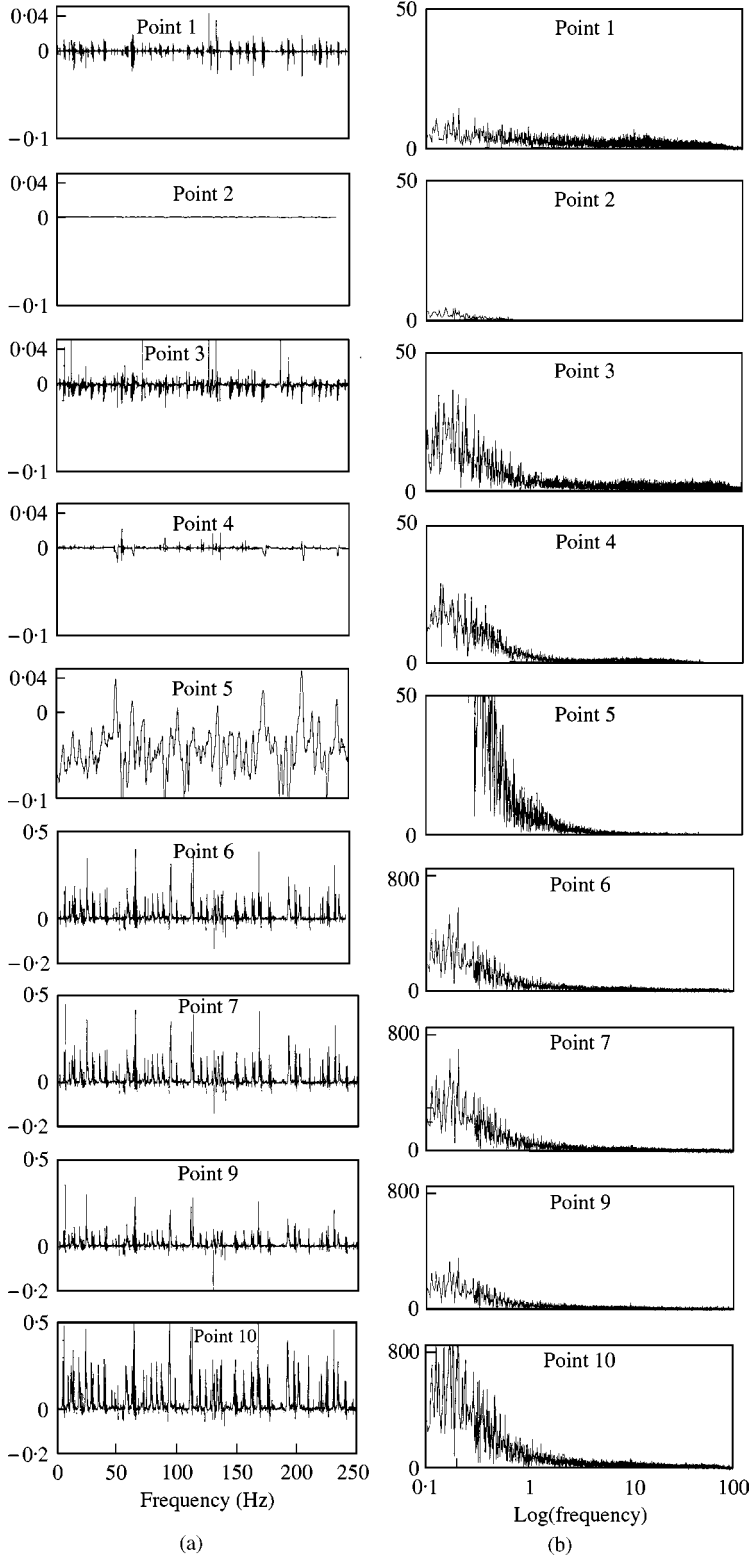
local flow acceleration attenuates the amplitude at higher frequencies above $\omega = 30$. The FFT of the time series for the Points 6, 7, 9 and 10 have been plotted in an enlarged scale, as compared to the other points. The response in the near-wake increases in the downstream direction as one moves from Point 3 to Point 10. Also, as one moves downstream, higher and higher frequencies are excited with higher amplitude. However, Points 7 and 10 that are neighbouring points have identical frequency bandwidth of the response.

The receptivity of the flow is such that the circular frequencies below 100, are only amplified. The constant tail in the FFT data beyond 100 is due to the input FST spectrum, i.e. the fluid dynamical system shows *buffeting* at higher frequencies. This also shows that the adopted numerical scheme is neutrally stable for even the highest resolved temporal and spatial scales. The exact receptivity of the flow is determined by the local shear layer properties. The band of frequencies that are amplified keeps increasing as one moves towards the trailing edge. This can be ascertained by comparing the Fourier amplitude of Point 1 with that of Point 4—the receptive frequency-band for Point 1 is almost double that of Point 4. The constant-amplitude tail, at higher frequencies, also increases as shear layer



Figure 4 (a). The curvilinear v-component of velocity at the sampled points shown as a function of time; (b) The Fourier transform shown against frequency for the time series of (a).
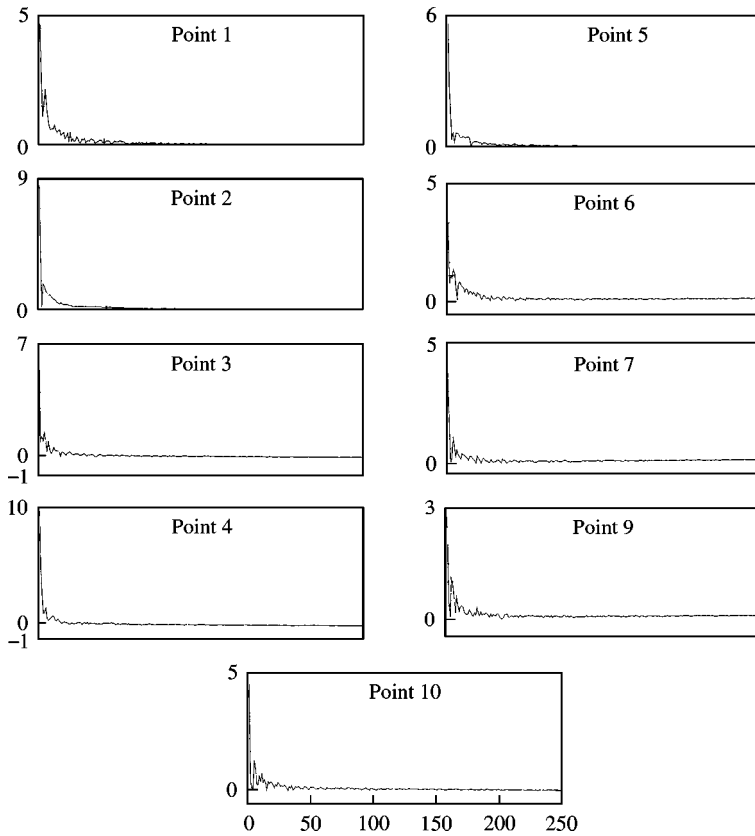
Figure 5. The Lyapunov exponent as a function of time for all the sampled points.

thickness increases, implying growth of disturbances in both space and time, for separated and free shear layer flows. It is to be noted that the buffeting amplitude for Point 3 is manifold as compared to that for Point 1. By looking at the excited frequency-bands, one can see two sets of points. Points 1, 3 and 4 belong to one, while all the points in the near-wake, belong to the other set—with Point 2 belonging to neither of the groups. Comparing the FFT of velocity-component signals for Points 5 and 4, one can understand the role of adverse pressure gradient. At Point 5, the flow is accelerated and one can see that the very low-frequency amplitudes are dominant and the receptive frequency-band is much narrower compared to that of Point 4. Point 2 has identical receptive frequency-band as compared to Point 5; however, the amplitude is 10 times lower for Point 2, due to its location close to the front stagnation point.

In Figure 4(a, b), the v-component time series and its FFT, are shown for the near-wake points. At these points, this component of velocity actually indicates the streamwise component of the response. The response is seen to be highly intermittent.

In Figure 5 the Lyapunov exponents, as a function of time, are displayed for all the sampled points. After an initial transient period, this exponent at all points reaches a steady-state small positive value, thus implying the flow to be chaotic at all points except Points 2 and 5, where the Lyapunov exponents are very small. Thus, Point 5 displays nonchaotic unsteadiness while Point 2 displays quasisteady nonchaotic behaviour. These figures also display that after $t = 80$, the Lyapunov exponents do not change with time.
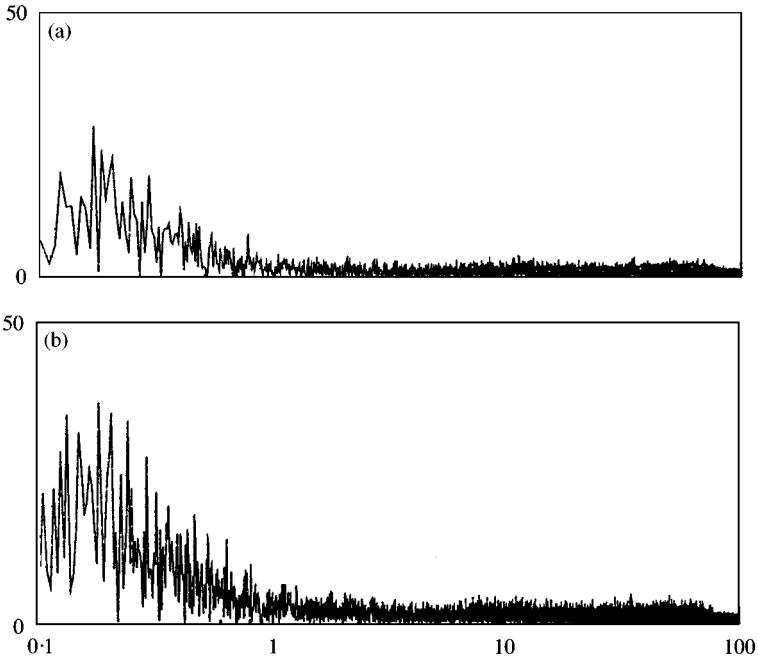
Figure 6. The Fourier transform of u-component of signal at Point 3 for (a) the time series up to $t = 150$; (b) the time series up to $t = 250$.

Thus, although the flow is strongly time dependent, a simulation up to $t = 80$ is enough to characterize its chaotic nature.

There is another aspect of unsteady flows which requires emphasizing. When one computes such a flow, it is necessary to find the time-period over which the flow should be computed, as the flow is aperiodic. To address the question, one should look for statistical stationarity of all flow variables. For this purpose, the FFT of the time series for the u-component is shown in Figure 6 for Point 3, for two different lengths of the signal, for the $Re = 100\,000$ and $\alpha = 30°$ case. The remarkable similarity, over a moderate and higher circular frequency range, of these two FFTs indicates that the dynamics is neither dissipative nor unstable in the numerical sense. The differences in the low-frequency range are due to the length of the signals; the longer the computational time, the more visible the lower frequencies will be. It establishes that taking the time series up to $t = 150$, is adequate to represent the frequency selection mechanism, i.e. the receptivity of the flow.

## 4.1. EFFECT OF ANGLE OF ATTACK FOR $Re = 100\,00$

Flow behaviour at this Reynolds number is investigated for an additional angle of attack ($\alpha = 5°$). It is seen from the time series that Points 1, 3, 4, 7, 9 and 10 exhibit intermittency for $\alpha = 30°$. At the lower angle of attack, the response is modulated at these points. Some representative figures are shown in Figure 7, for the $\eta$-component of velocity, the FFT and the time dependence of the Lyapunov exponent. Points 3 and 10, being in the near-wake,

Figure 7. The v-component of velocity; its Fourier transform and Lyapunov exponent for Points 2,3 and 10 for $Re = 100\,000$ and $\alpha = 5°$.
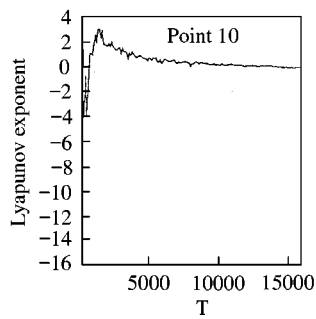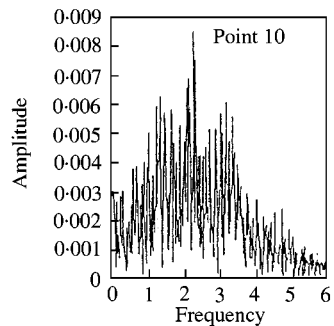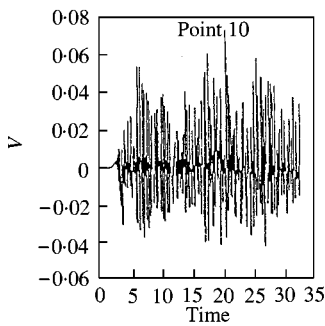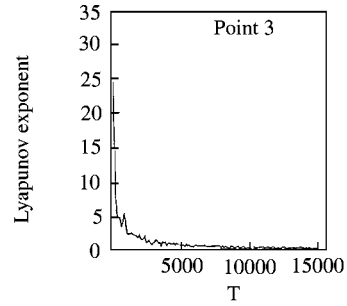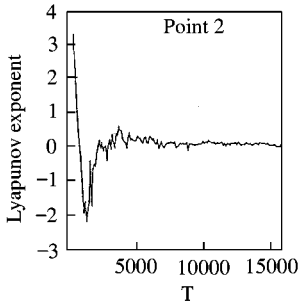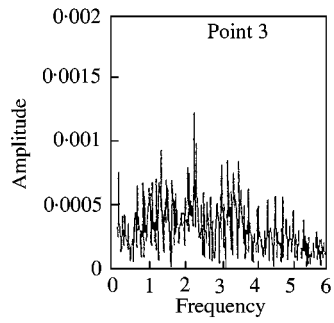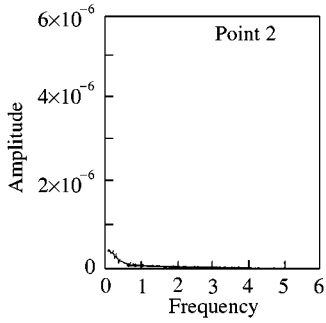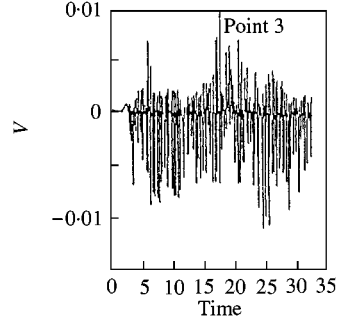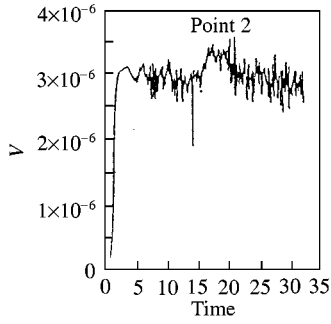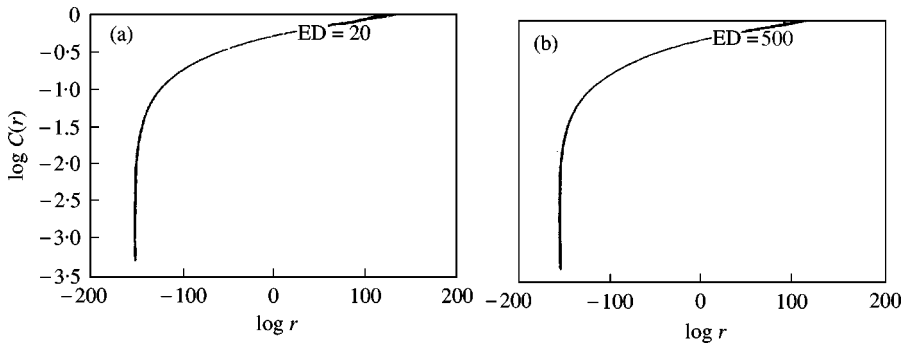
Figure 8. Correlation dimension for flow past NACA 0015 airfoil for $\alpha = 30°$ and Re $= 100\,000$ for FST level of 5% for Point 1 with maximum embedding dimensions: (a) ED $= 20$ and (b) ED $= 500$.

show similar disturbance spectra with the magnitude increasing in the downstream direction for both angles of attack. Another distinct feature for the lower angle of attack case is that the output is more broadband. Also, Point 2 shows certain time intervals when the Lyapunov exponents take negative values for the $\alpha = 5°$ case, i.e. during these time intervals the flow is temporally stable.

The calculated flows, for chosen parameter values, are chaotic and the degree of chaos can be obtained from calculated dimensions of the system. The correlation dimension, $d_c$, is the most physically suitable one to characterize the chaotic dynamical system. It is obtained as a slope of correlation integral ($C$) evaluated from the embedded vector plotted against the separation distance ($r$), as shown in Figure 8, for two values of chosen embedding dimension. Both cases reveal that the value of $d_c$ is approximately equal to 600. The practical reason for calculating this dimension is to reduce the governing partial differential equations to a set of ordinary differential equations in time–known as reduced order modelling (Dowell 1996). This can be done either through eigenvalue and eigenvector expansion or through a proper orthogonal decomposition (POD) method considering only the most energetic modes. There can also be the alternative statistical route, where the probability distribution function (PDF) of the velocity signal can be used to reproduce a time series by statistical methods as we have done for synthesizing the time series for the FST at the inflow boundary. The latter approach can be gainfully employed for the purpose of flow control also.

## 4.2. The Intermittency Factor

Having obtained the time series at the sampling points over a time period, when effects of transients have decayed, it is possible to estimate the intermittency factor at these points. To distinguish between the laminar and the turbulent nature of the flow at a given spatial location one needs to have a good discriminator between the two types of flow. This then becomes a problem of signal processing and was tackled previously by experimentalists. While this is discussed in Hedley & Keffer (1974), Ramesh et al. (1996) used a simpler method of calculating the intermittency distribution for a three-dimensional constant-pressure, diverging flow, by obtaining the PDF of the squared second time-derivative of the velocity signal. In this work following the same method, the second derivative of the signal is evaluated by a fourth-order accurate method to minimize undue attenuation of the signal at higher frequencies. This is superior to the second-order method that filters the frequency spectrum at higher frequencies. For the same reason, it is also known that instead of the
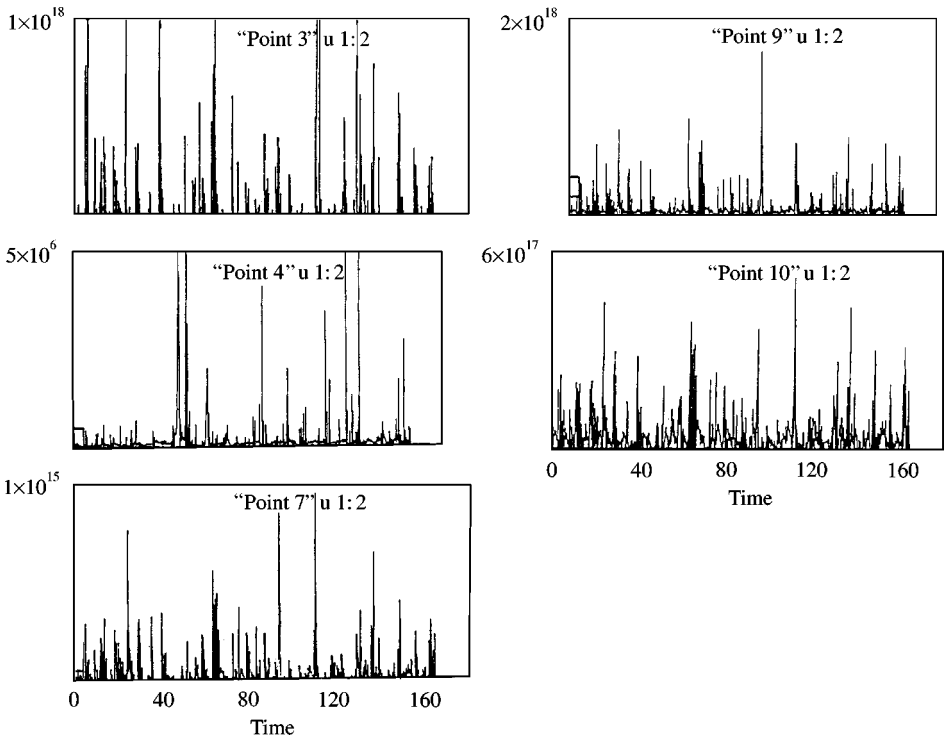
Figure 9. The time variation of $D_\omega(= \mathrm{d}^2\omega/\mathrm{d}t)$ constructed from the vorticity signal for Re = 100 000 and $\alpha = 30°$ for some representative points.

velocity signal, if one uses instantaneous wall shear stress then the distinction between the laminar and the turbulent flow becomes sharper (Schneider 1995). Here both the velocity and vorticity (which is proportional to the local shear stress) time series have been used to compute the intermittency factors at various sampling points, but only the vorticity signal results are shown. In Figure 9, the time variation of $D_\omega = \mathrm{d}^2\omega/\mathrm{d}t$, for some of the sampling points is shown for the Re = 100 000 and $\alpha = 30°$ case. In Figure 10, the PDFs are shown for some of the points and the distinct break in the curves indicates the threshold level discriminating the turbulent from the laminar flow. The frequency of occurrence of any event is plotted along the ordinate as a function of the exponent of the value of $D_\omega$ (to the base ten). In calculating the frequency of occurrence, a bin-width of 1·0% has been used around the chosen central values. The overall appearance and the values of PDF are sensitive to the choice of the bin-width, but the break in the curve indicating the threshold of turbulence more or less remains the same and so does the intermittency value. Note that Points 2 and 4 are near the front stagnation point and the most likely $D_\omega$ values are three to four times lower at these points compared to other points—except Point 5, where a very high value of $D_\omega$ is achieved because of strong local acceleration. For Point 1, the threshold is close to $10^{16.75}$, while the flow is not turbulent at Point 2. Point 3, being in the near-wake, the PDF indicates an earlier break at $10^{15.90}$—but this is not a very clear one. Also note that the highly intermittent signal shows up in terms of a long tail beyond $10^{17}$, and this is due to the already-mentioned *buffeting* in the frequency spectrum. For Point 4, which is located near the maximum adverse pressure gradient, the threshold is at $10^{15.5}$; Point 5 is also characterized by low-frequency oscillation and once again the flow is not turbulent. Points 6 and 7 are also in the near-wake but are further downstream than point 3 and for
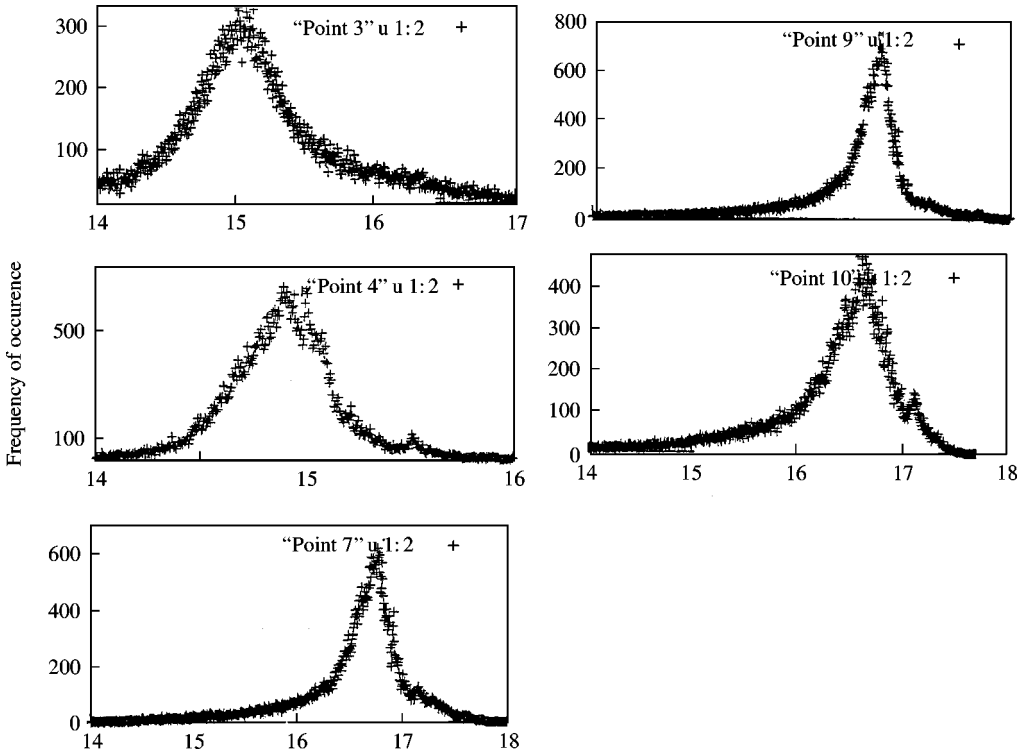
Figure 10.  The probability distribution function (PDF) for the computed vorticity field for the data shown in Figure 9.

TABLE 3
Intermittency factor for Re = 100 000 and $\alpha = 30°$

| Points | Threshold | Intermittency factor |
|--------|-----------|----------------------|
| 1  | $10^{16 \cdot 75}$ | 0·1233 |
| 3  | $10^{15 \cdot 90}$ | 0·1384 |
| 4  | $10^{15 \cdot 5}$  | 0·0528 |
| 6  | $10^{17 \cdot 1}$  | 0·0832 |
| 7  | $10^{17 \cdot 1}$  | 0·0877 |
| 8  | $10^{15 \cdot 5}$  | 0·1210 |
| 9  | $10^{17 \cdot 0}$  | 0·0966 |
| 10 | $10^{17 \cdot 0}$  | 0·0851 |

these points the threshold also increases to $10^{17 \cdot 1}$. The threshold values at the sampling points are indicated in Table 3.

From the information in Figure 10 and the threshold values in Table 3, one can easily calculate the intermittency factors by using a binary decision, i.e. one can create a function $I(t)$ which takes a value equal to one if the instantaneous $D_\omega$ value is greater than the threshold value, and is otherwise set equal to zero. Once this function $I(t)$ is evaluated, the intermittency factor is obtained from

$$\gamma = \frac{1}{T} \int_0^T I(t)\, dt, \tag{15}$$

where $T$ is the total sampling time. The calculated intermittency factors are also shown in Table 3. The threshold values are not the same for all the points, because the underlying shear flows are qualitatively different and hence for the same reason one cannot use a universal model for transition for all the points. The fact that the threshold values are not easily detected, is due to the low values of Reynolds number for which computations are performed. For the present exercise it is only for Points 4, 7 and 10 that the thresholds are clearly detected from the PDF. The intermittency factors can also be obtained from the same time series by progressively taking longer and longer time segments, always starting from the beginning. In doing so, it was found that the intermittency factors did not change anymore beyond $t = 140$. This is in conformity with the statistical stationarity that was discussed earlier. Also, the values of intermittency obtained were in the predictable range depending on the location and the nature of the shear layer.

## 5. CONCLUSIONS

Unsteady flow past a NACA 0015 aerofoil section is investigated for moderate Reynolds numbers, at high angles of attack, by solving the full Navier–Stokes equations in the presence of Free Stream Turbulence, which is modelled by a Moving Average time-series model. This is a novel approach for studying the effect of FST on bluff-body flows in the transitional flow regime, and the numerical results should be viewed as the first set of very accurate simulation recording the effect of FST in triggering *by-pass* transition. Another reason for undertaking the present research was to explore the possibility of using reduced-order modelling of bluff-body flows for aeroelastic applications. This was attempted by using dynamical system tools and it is shown that the correlation dimension is very high—of the order of six hundred, i.e. the governing partial differential equation can be replaced by that many coupled ordinary differential equations. Therefore, this does not appear to be an attractive proposition. Physically, it is also seen that different parts of the flow past the aerofoil at high angles of attack show entirely different flow behaviour; this then precludes the eigenfunction expansion route. In this exercise the intermittency due to a very large number of bifurcations suffered by the flow in the presence of FST is computed and this information can be used to embed transitional flow information in turbulence models.

## REFERENCES

ATASSI, H. M. 1994 Unsteady aerodynamics of vortical flows: early and recent developments. Proceedings of *Symposium on Aerodynamics & Aeroacoustics* (ed. K. Y. Fung), pp. 121–171. Singapore: World Scientific.

BAKER, G. L. & GOLLUB, J. P. 1996 *Chaotic Dynamics—An Introduction*, 2nd edition. Cambridge: Cambridge University Press.

BATCHELOR, G. K. & TOWNSEND, A. A. 1947 Decay of vorticity in isotropic turbulence. *Proceedings of the Royal Society* (*London*) A **191,** 534–550.

DOWELL, E. H. 1996 Eigenmode analysis in unsteady aerodynamics: reduced order models. *AIAA Journal*, **34,** 1578–1583.

FENSTERMACHER, P. R., SWINNEY, H. L. & GOLLUB, J. P. 1979 Dynamical instabilities and the transition to chaotic Taylor vortex flow. *Journal of Fluid Mechanics* **94,** 103–128.

FORTIN, A., FORTIN, M. & GERVAIS, J. J. 1987 A numerical simulation of the transition to turbulence in a two dimensional flow. *Journal of Computational Physics* **70,** 295–310.

FRIGO, M. & JOHNSON, S. G. 1997 The fastest Fourier transform in the west. MIT Technical Report number # MIT-LCS-TR-728. Also in *Proceedings of 23rd International Conference on Acoustics, Speech & Signal Processing,* vol. 3, p. 1381 (1998).

FRISCH, U. 1995 *Turbulence: A Legacy of A. N. Kolmogorov.* Cambridge: Cambridge University Press.

FULLER, W. A. 1978 *Introduction to Statistical Time Series.* New York: Wiley.

GOLLUB, J. P. & SWINNEY, H. L. 1975 Onset of turbulence in a rotating fluid. *Physical Review Letters* **1,** 927–930.

HEDLEY, T. B. & KEFFER, J. F. 1974 Turbulent/non-turbulent decision in an intermittent flow. *Journal of Fluid Mechanics* **64,** 625–644.

LEGRAS, B. & DRITSCHELL, D. 1993 Vortex stripping and the generation of high vorticity gradients in two-dimensional flows. *Applied Scientific Research* **51,** 445–455.

MORIKAWA, K. & GRONIG, H. 1995 Formation and structure of vortex systems around a translating and oscillating aerofoil. *Zeitschriftfür Flugwissenschaften und Welttraumforschung* **19,** 391–396.

NAIR, M. T. & SENGUPTA, T. K. 1997 Unsteady flow past elliptic cylinders. *Journal of Fluids and Structures* **11,** 555–595, doi:10.1006/jfls.1997.0095

NAIR, M. T. & SENGUPTA, T. K. 1998 Orthogonal grids for the solution of Navier-Stokes equation. *International Journal for Numerical Methods in Fluids* **28,** 215–224.

PULLIAM, T. H. & VASTANO, J. A. 1993 Transition to chaos in an open unforced 2D flow. *Journal of Computational Physics* **105,** 133–149.

RAMESH, O. N., DEY, J. & PRABHU, A. 1996 Transitional intermittency distribution in a three-dimensional constant pressure diverging flow. *Experiments In Fluids* **21,** 259–263.

SCHNEIDER, S. P. 1995 Improved method for measuring laminar-turbulent intermittency in boundary layers. *Experiments In Fluids* **18,** 370–375.

SENGUPTA, T. K. & NAIR, M. T. 1999 Upwind Schemes and LES. *International Journal for Numerical Methods in Fluids* **31,** 889–899.

SENGUPTA, T. K., ZHENGYI, W., YEO K. S. & CHATTOPADHYAY, M. 1999 Receptivity to convected vortices—by-pass route. In *Proceedings of 8th Asian Congress of Fluid Mechanics* (ed. E. Cui), pp. 964–968. Beijing: International Academic Publishers.

VASTANO, J. A. & MOSER, R. D. 1991 Short-time Lyapunov exponent analysis and transition to chaos in Taylor-Couette flow. *Journal of Fluid Mechanics* **233,** 83–118.

WOLF, A., SWIFT, J. B., SWINNEY, H. L. & VASTANO, J. A. 1985 Determining Lyapunov exponents from a time series. *Physica 16D,* **16,** 285–317.

WU, X., JACOBS, R. G., HUNT, J. C. R. & DURBIN, P. A. 1999 Simulation of boundary layer transition induced by periodically passing wakes. *Journal of Fluid Mechanics,* **399,** 109–153.